ISSN 0036-0236, Russian Journal of Inorganic Chemistry, 2023, Vol. 68, No. 11, pp. 1582–1591. © Pleiades Publishing, Ltd., 2023.
Russian Text © The Author(s), 2023, published in Zhurnal Neorganicheskoi Khimii, 2023, Vol. 68, No. 11, pp. 1588–1598.

THEORETICAL
INORGANIC CHEMISTRY

Dedicated to the 300th anniversary of St. Petersburg University

Derivation of a Force Field for Computer Simulations of Multi-Walled Nanotubes Using Genetic Algorithm. I. Tungsten Disulfide

A. V. Bandura[a], *, S. I. Lukyanov[a], A. V. Domnin[a], D. D. Kuruch[a], and R. A. Evarestov[a]

[a] *Quantum Chemistry Department, Saint-Petersburg State University, St. Petersburg, 199034 Russia*

**e-mail: a.bandura@spbu.ru*

Received June 6, 2023; revised June 29, 2023; accepted July 7, 2023

Abstract—A technique for constructing force fields based on the use of genetic algorithms is proposed, which is aimed at parameterization of potentials intended for computer simulation of polyatomic nanosystems. To illustrate the proposed approach, a force field has been developed for modeling layered modifications of WS_2, including multi-walled nanotubes, the dimensions of which are beyond the capabilities of ab initio methods. When determining the potential parameters, layered polytypes of bulk crystals, monolayers, bilayers, and nanotubes of small diameters were used as calibration systems. The parameterization found was successfully tested on double-walled nanotubes, the structure of which was determined using density functional calculations. The obtained force field was used for the first time to model the structure and stability of achiral multi-walled nanotubes based on WS_2. The interwall distances obtained from the simulation are in good agreement with the results of recent measurements of these parameters for existing nanotubes.

Keywords: interatomic potentials, multiobjective optimization, genetic algorithms, multi-walled nanotubes, DFT calculations

DOI: 10.1134/S003602362360209X

INTRODUCTION

In the last twenty years, the studies of low dimensional materials, namely 2-D and 1-D structures, have given rise to new scientific and engineering fields of knowledge. This is due to the fact that 2-D nanolayers (mono- and multilayers, misfit compounds), as well as 1-D materials (nanotubes (NTs), nanorods) have properties that differ essentially from the properties of the 3-D materials [1]. Thus, nanotubes obtained from tungsten disulfide, because of their 1D structure, demonstrate unique thermoelectric properties [2], enlargement of the bulk photovoltaic effect [3], resistance to high pressure [4], enhancement of the light-matter interactions [5]. These and other characteristics allow WS_2 nanotubes to find application in a wide range of engineering solutions. In particular, WS_2-based nanotubes are used for designing sensors [6], field effect transistors [7–9], optoelectronic [10, 11] and thermoelectric [2] devices and also for developing high frequency torsional nanoelectromechanical resonators [12]. Besides that, WS_2 NTs are used to reduce friction (as solid-state lubricant) [13], and due to their excellent mechanical properties and high impact resistance, WS_2 NTs are a promising nanomaterial that improves the characteristics of various nanocomposite polymers [14–16].

It was shown experimentally [17] that WS_2 nanotubes are multi-walled, have from 20 to 40 walls, an outer diameter of 40–150 nm, and a length of 1–10 μm. In recent years, efficient methods for the synthesis of high quality WS_2 nanotubes have been developed [18–20]. The WS_2 NTs obtained using these methods have a relatively high degree of crystallinity; their diameters are distributed in a narrow interval from 30 to 120 nm with a mean value of 70 nm and an aspect ratio >100 [20]. The high degree of crystallinity permits very accurate measurements of the WS_2 NT interwall distance (6.242 Å) [20]. Special synthesis methods make it possible to obtain "thin" WS_2 NTs with a diameter of 20 ± 2.3 nm and a number of walls of 9 ± 2 [18]. In Ref. [21] a high-resolution transmission electron microscopy (HRTEM) image of a triple-walled nanotube is presented. The nanotubes with four [22] and five [23, 24] walls are also investigated. Both achiral armchair and zigzag nanotubes [22, 25] and chiral samples [23, 24] have been described.

It has been shown that the electronic structure and optical properties of WS_2 NTs depend on such structural characteristics as the diameter and number of walls [5, 26, 27]. In the process of studying WS_2 NTs [22, 27], various methods of structure modeling were

used. At the same time, the most powerful modeling tool, quantum-chemical calculations, is applicable only to very thin and maximally triple-walled nanotubes based on metal chalcogenides [28–33]. To simulate multi-walled nanotubes (MWNTs) containing thousands of atoms in a primitive cell, force fields are employed (see, for example, articles [31, 34] of the authors of this work and references therein).

In this paper, we present a method for calibrating the force field using multi-objective optimization via genetic algorithms and obtain a new force field that describes the interactions of atoms in crystalline systems, nanolayers, and nanotubes based on WS_2. To calibrate the atomic potentials both experimental data and the results of quantum-chemical calculations have been used. The principles of the force field design are described in the next section.

The Results and Discussion section describes the process of testing the force field on single-wall (SWNT) and double-walled (DWNT) nanotubes by comparing the results of molecular-mechanical (MM) modeling and quantum-chemical (QC) calculations. In the same section, the results of using the obtained force field for modeling WS_2 NTs with the number of walls from 1 to 5 and the outer diameter from 12 to 191 Å are described.

COMPUTATIONAL DETAILS

Quantum-Chemical Calculations

The QC calculations were performed within the framework of the density functional theory (DFT) according to the procedure adopted in our previous works [29, 30]. For calculations we used the licensed computer program CRYSTAL17 [35, 36], in which Gaussian atomic orbitals are used to construct the basis of the Bloch functions. For purpose to take into account the interactions between the core and valence electrons of the S atom, as well as core, valence and sub-valence electrons of the W atom, the relativistic pseudopotentials CRENBL [37, 38] were used.

The hybrid exchange-correlation functional HSE06 [39] was chosen for calculations. The Brillouin zone sampling was performed using Monkhorst Pack meshes [40] comprising of $18 \times 18 \times 10$, 18×18, and 18 $\boldsymbol{k}$-points for bulk, monolayer and nanotubes based on WS_2, accordingly. One-electron equations were solved iteratively to self-consistency in energy within a threshold of 3×10^{-9} eV.

To reproduce van der Waals interactions between layers in a bulk crystal, as well as between walls in multi-walled nanotubes, the dispersion correction was included in the calculation using the DFT-D2 approximation [41].

A more detailed description of the applied methodology is published in the articles [29, 30].

Choice of Force Field Interatomic Potentials

The choice of the functional dependence of the contributions to the potential energy is most important stage of the force field designing. In this work, we adopted the potential model [31] proposed by us earlier for modeling multi-walled nanotubes based on MoS_2. This model consists of four types of potentials: 1) the Coulomb potential expressed through the effective charges on atoms; 2) two-body Morse potential referred to short-range interactions W-S and W-W; 3) the Buckingham potential representing pair interactions between sulfur atoms; 4) three-body Stillinger-Weber potential, which provides contribution of three-body interactions concerned with valence angles WSW. All the mentioned potentials are realized in the freely distributed GULP program [42] intended both for molecular-mechanics and molecular-dynamics simulations and also for calibration of potential parameters. The particular form of the potentials employed is indicated in the Ref. [31] and also presented in electronic form in the Supplementary Materials. The found values of the empirical parameters are given in Table S1. Also in Supplementary Materials, the results of molecular-mechanical calculations of the properties of the calibration systems are compared with their reference values (Tables S2 and S3). This potential model has proven itself well [31] in modeling the structure and properties of bulk phases, monolayers, single-wall and multi-walled nanotubes based on MoS_2.

However, when testing the above potential model, it turned out that it incorrectly conveys the relative energy of the $2H$ and $1T$ bulk phases of MoS_2, significantly overestimating the stability of the latter. This circumstance leads to incorrect results of molecular-dynamics modeling of multi-walled nanotubes at elevated temperatures. To eliminate the mentioned shortcoming an additional three-body potential was introduced into this potential model. This additional term reduces the relative advantage of the octahedral coordination of the metal atom with respect to the trigonal-pyramidal coordination actually realized in WS_2 layers. This potential is taken from the ESFF force field [43] and reflects the angular dependence of the energy on valence angles close to 0°, 90°, or 180°. In the GULP program [42] this potential is designated as Linear-three-body (LTB). In the present work the following form was used:

$$V_3^{\mathrm{LTB}} = k\left[1 + \cos\left(4\theta\right)\right], \qquad (1)$$

where θ is the SWS valence angle and k is an empirical constant.

Force Field Calibration Method

In this study, the EZFF library [44] was employed to refine the force field parameters. This library is designed for multicriteria optimization of force fields and, notably, it is not bound to a particular molecular

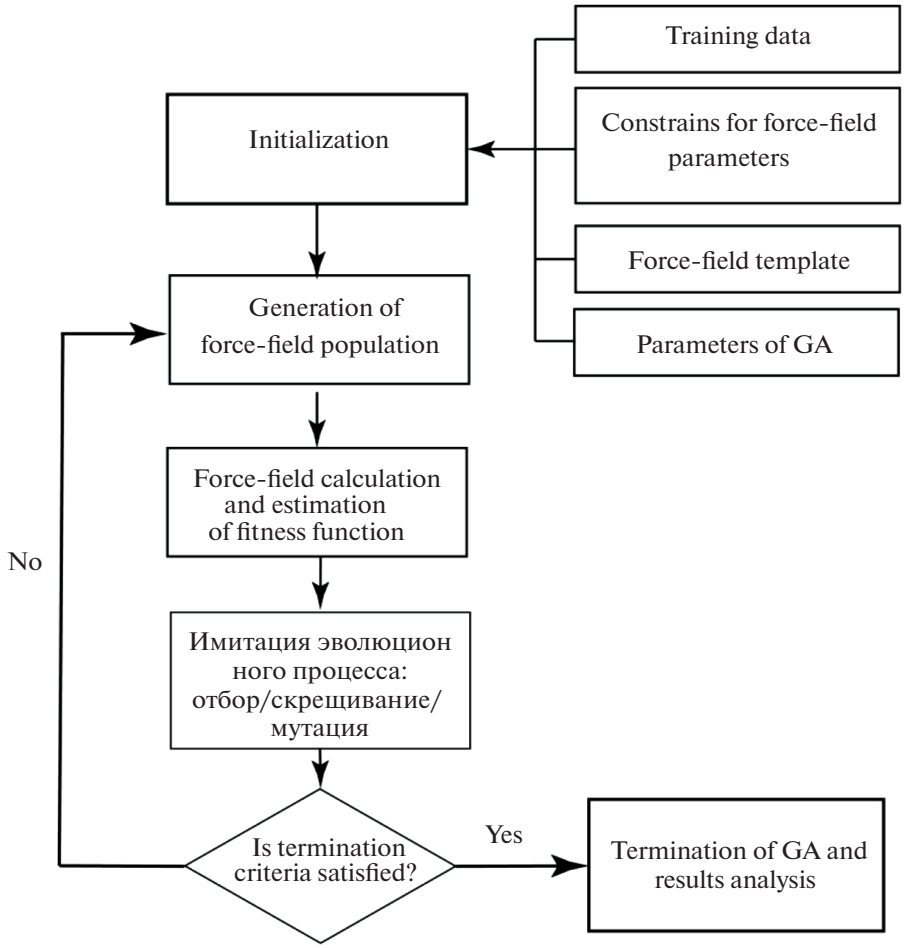

Fig. 1. General scheme of the force field optimization process.

mechanical program; it can interface with various programs such as GULP [42], RXMD [45], among others. An additional key advantage of this library is its open distribution and accessibility through open-source code, which allows users to modify it in accordance with the provided license. Notably, the EZFF library is developed in the Python3 programming language. To facilitate its functionality, the EZFF library leverages the genetic algorithms implementation provided by the Platypus package [46].

The seaborn [47] and matplotlib [48] libraries were employed for visualizing the results. Processing and analysis of the acquired force fields were conducted using the Pandas [49] and scikit-learn [50] libraries.

To initiate the functionality of EZFF, several parameters of the genetic algorithm must be defined. These include the number and size of generations, as well as the magnitude of mutations. Additionally, the specification of a force field template file and a file detailing acceptable parameter range are essential. Furthermore, the setting of objective functions for optimization is imperative. To achieve this, model structures and their corresponding physical properties should be explicitly defined. The overarching operation scheme of EZFF is depicted in Fig. 1.

Rather than minimizing the error of each characteristic of the considered structures individually, the approach was taken to categorize them into distinct groups. The following five groups were identified: 1) lengths of lattice translation vectors, 2) angles between lattice translation vectors, 3) elasticity characteristics (including Young's modulus and elements of the elasticity tensor), 4) phonon frequencies, and 5) relative values of total energy. For each of these groups, error calculations were conducted utilizing the Mean Absolute Percentage Error (MAPE) function, which is computed according to the following formula:

$$\mathrm{MAPE}\left(y,\hat{y}\right)=\frac{1}{n}\sum_{i=1}^{n}\frac{\left|y_i-\widehat{y_i}\right|}{\max\left(\epsilon,\left|y_i\right|\right)}, \qquad (2)$$

where $\widehat{y_i}$ represents the calculated value of the i-th parameter, y_i denotes its true value acquired experimentally or theoretically, a ϵ is a chosen small, strictly positive value employed to prevent singularity when $y_i = 0$.

The MAPE function exhibits sensitivity to relative errors, a characteristic particularly advantageous for identifying errors in oscillation frequencies. This is noteworthy because as the frequency decreases, its impact on the overall error becomes more noticeable.

In this study, the process of optimizing the force field was undertaken in several stages:

— initial scanning of the parameter space to broadly identify regions where potential parameters exhibit optimality;

— evaluation of the obtained results, identification of optimal force fields, and their categorization into groups based on the principle of highest similarity;

— subsequent refinement of force field parameters within each group, incorporating a more extensive range of model systems.

Out of all the fields acquired during the optimization process, the top 1% of fields with the most favorable objective function values were chosen. These selected fields then underwent the final stage of optimization using the gradient descent method within the GULP program [42].

Although the EZFF algorithm does not directly address the primary issue of generating sets of preestablished force fields, this approach aids in identifying favorable initial approximations. The existence of these approximations significantly streamlines the process of developing a field suitable for modeling nanosystems.

Calibration Systems

The set of calibration (training) systems is determined by the objects of the supposed simulation – multi-walled nanotubes based on WS_2. Apparently, most of the physical properties of nanotubes are potentially contained in the properties of the original layered crystals, since nanotubes, in fact, reproduce the same structure, but in a different "folded" supramolecular geometry. Therefore, two stable phases (2*H* and 3*R*) of tungsten disulfide, as well as its isolated monolayers, were included in the list of the reference systems. Furthermore, for the above reasons, the hypothetical 1*T* phase, in which the metal atom has octahedral coordination, was added to the real phases. The set of reference properties included lattice constants, atomic coordinates, elastic constants, W–S chemical bond lengths, SWS, WSW valence angles, and (limited) sets of phonon frequencies at various points of the Brillouin zone. For most of the indicated quantities, experimental values were used. In cases where experimental data were not available, the results of quantum chemical calculations were used (see below).

To reproduce in a most correct manner the dependence of the interwall interaction energy on the interwall distance in multi-walled nanotubes, six pairs of monolayers were added to the calibration systems. These monolayers were positioned one with respect to another at different distances and with different displacements and orientations corresponding to different stacking of monolayers in the 2*H* and 3*R* phases [51]. Besides of this, two nanotubes with minor diameters were included: one nanotube of the "armchair" chirality (6, 6) and the other of the "zigzag" chirality (12, 0). For the mentioned systems the reference quantities were the lattice constants and the atomic positions which have been found by the DFT method. For nanotubes, the first six frequencies at the center of the Brillouin zone were additionally calculated and included in the training set to ensure the absence of imaginary frequencies and the correct reproduction of the lowest frequencies.

For all of the aforementioned calibration systems, the quantum-chemically calculated (potential) energy of formation from the bulk 2*H* phase was included as a reference property.

The final values of the empirical parameters are given in the Supplementary Materials. The average deviations from the reference values corresponding to the obtained parameterization of the considered force field are also indicated there.

RESULTS AND DISCUSSION

Testing the Proposed Force Field

The developed force field was tested on single-wall and double-walled nanotubes calculated in advance using the quantum–chemical method described in the preceding section.

The energy stability of nanotubes is traditionally estimated from the strain energy (E_{str}) calculated relative to the monolayer's energy:

$$E_{str} = E_{NT}/N_{NT} - E_{mono}/N_{mono}, \quad (3)$$

where E_{NT} and E_{mono} are the total energies of the NT and the monolayer calculated per unit cell. The values N_{NT} and N_{mono} (=1) are the corresponding numbers of formula units.

The dependences of the strain energies on the average diameters of nanotubes calculated through a force field are compared with the same dependences obtained by the quantum-chemical method in Fig. 2. In this case, achiral nanotubes of the "armchair" and "zigzag" types with a diameter in the range of 10–40 Å are considered. The average diameter D_{NT} of nanotubes was calculated as the sum of (average) radii of cylinders corresponding to the positions of sulfur atom centers on the inner and outer shells. As can be seen from Fig. 2, the agreement between the molecular-mechanical and quantum-chemical quantities is quite good: the absolute error is 3–5 kJ/mole.

To confirm the applicability of a force field in modeling multi-wall nanotubes, double-walled achiral nanotubes with an outer diameter in the range of 30–40 Å were calculated both quantum-chemically and within the framework of a force field. The geom-

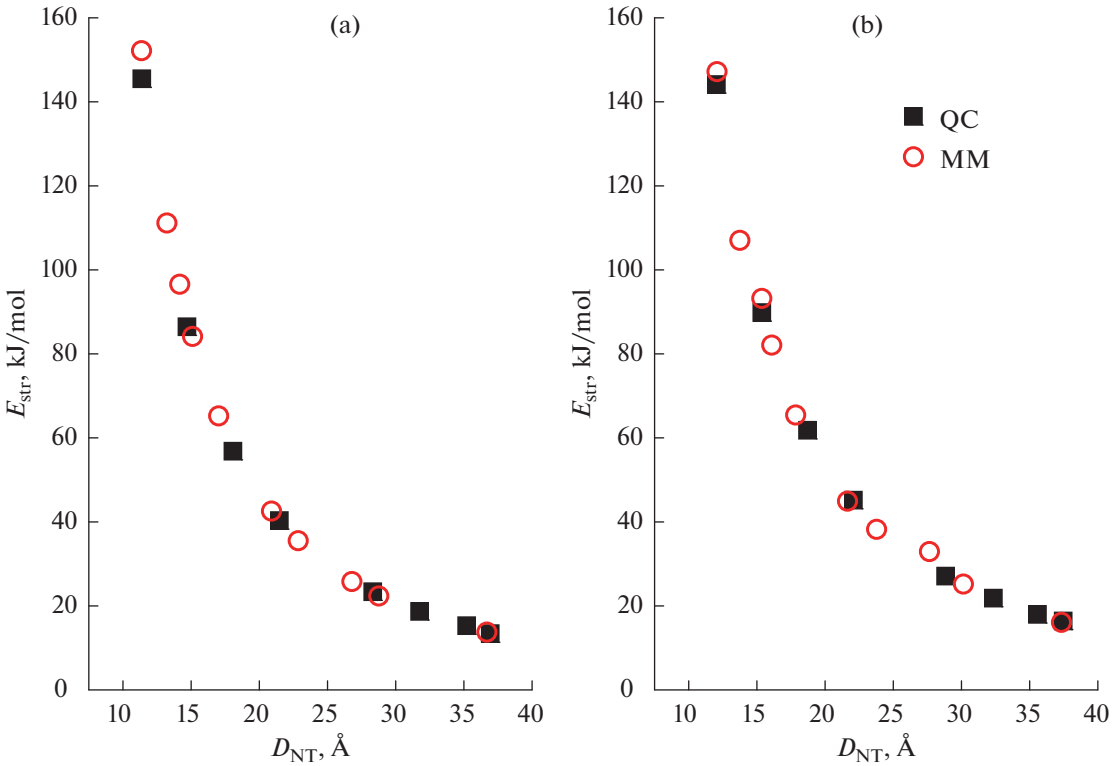

Fig. 2. Dependences of the strain energy of single-wall nanotubes WS_2 on the average diameter: (a) "armchair" tubes; (b)—"zigzag" tubes. Designations: MM—results of calculations with the help of a force field; QC—results of quantum chemical calculations.

etry of double-walled tubes of the "armchair" $(n_1, n_1)@(n_2, n_2)$ and "zigzag" $(n_1, 0)@(n_2, 0)$ types was optimized. The initial structures of the tubes were created by combining two single-wall nanotubes with the same chirality type and different average diameters D_{n_2} and D_{n_1} under the constraints that the initial interwall spacing $\Delta R_{NT} = (D_{n_2} - D_{n_1})/2$ was from 5 to 7 Å. Simultaneously, the chirality indexes n_1 and n_2 were selected in such a way that, at a fixed interwall distance, they had the greatest common devisor n. Such a choice provides greatest symmetry of the double-walled tube and, as a consequence, reduces computational costs.

As is known [29], single-wall achiral nanotubes rolled up from tungsten disulfides belong to the 4th ("armchair" type) or 8th ("zigzag" type) family of one-periodic groups, and they lack a second-order rotation axis perpendicular to tube axis In fact, this corresponds to the possibility of two different orientations in the monolayers' stacking in WS_2 bulk phases. Therefore, calculations of double-walled tubes were performed in two variants: $2H$–stacking and $3R$–stacking, which correspond to either the same or opposite orientation of two single-wall components rolled up from the same monolayer.

For comparison of the stability of tubes with different interwall distances the binding energy E_{bind} was calculated. The binding energy indicates the energy gain (per formula unit) achieved by combining two SWNTs into one DWNT. This quantity reflects the contribution of interwall interactions to the energy of a double-walled tube and is defined by the following manner:

$$E_{bind} = \left(E_{DWNT} - E_{SWNT_1} - E_{SWNT_2}\right)/N_{DWNT}, \quad (4)$$

where E_{DWNT}, E_{SWNT_1}, E_{SWNT_2} are the energies of the DWNT and single-wall components, respectively, referred to one translational unit, while N_{DWNT} is the number of formula units in the DWNT unit cell. The calculated criteria for the stability of double-walled nanotubes also include the energies of formation of a DWNT from a bulk crystal (E_{form}) and from a monolayer (E_{str}). The formation energy relative to the energy of a bulk crystal,

$$E_{form} \equiv E_{form}^{bulk} = E_{DWNT}/N_{DWNT} - E_{bulk}/N_{bulk}, \quad (5)$$

is perhaps the most practically significant criterion for the stability of nanotubes. In formula (5) E_{bulk} is the calculated energy of one unit cell of the most stable WS_2 crystalline $2H$–phase containing N_{bulk} (= 2) formula units. The strain energy,

$$E_{str} \equiv E_{form}^{mono} = E_{DWNT}/N_{DWNT} - E_{mono}/N_{mono}, \quad (6)$$

Table 1. Binding energy (E_{bind}), formation energy from monolayer (E_{str}), formation energy from bulk crystal (E_{form}), and interwall distance (ΔR_{NT}) in double-walled nanotubes with "armchair" (n, n) and "zigzag" (n, 0) chirality. Quantum chemical (QC) and molecular mechanical (MM) results

Chirality	Δn	E_{bind}, kJ/mol		E_{str}, kJ/mol		E_{form}, kJ/mol		ΔR_{NT}, Å	
(n, n)	–	QC	MM	QC	MM	QC	MM	QC	MM
(12, 12)@(18, 18)	6	–2.7	–5.7	24.6	25.5	47.2	49.7	6.0	5.9
(14, 14)@(21, 21)	7	–8.1	–10.4	12.0	13.2	34.5	37.4	6.3	6.1
(12, 12)@(20, 20)	8	–8.2	–9.6	16.5	18.5	39.1	42.8	6.6	6.3
(12, 12)@(21, 21)	9	–4.2	–7.1	19.0	19.8	41.5	44.1	7.3	7.4
(n, 0)	–	QC	MM	QC	MM	QC	MM	QC	MM
(11, 0)@(22, 0)	11	–2.8	–8.0	63.9	59.0	86.5	83.2	5.8	5.8
(12, 0)@(24, 0)	12	–8.0	–11.2	49.1	46.5	71.7	70.7	6.0	5.9
(13, 0)@(26, 0)	13	–9.0	–10.8	40.4	39.4	63.0	63.6	6.3	6.1
(14, 0)@(28, 0)	14	–7.5	–8.4	35.5	35.7	58.0	60.0	6.6	6.4

can be directly compared with the strain energy for single-wall nanotubes of close diameter.

Table 1 presents the numerical values of the properties listed above, obtained as a result of quantum-chemical and molecular-mechanical calculations. Quantum-chemical calculations have shown that the dependence of the total energy of double-walled nanotubes on the wall stacking is negligibly small (does not exceed 0.1 kJ/mole). Therefore, Table 1 presents the values obtained for tubes, both components of which are rolled up from the monolayer in the same orientation. The agreement between quantum-chemical and molecular-mechanical calculations can be considered satisfactory. For the formation energies the difference between the values obtained using both approaches comprises on average 2 kJ/mole and does not exceed 5 kJ/mole. For the binding energies the average error in molecular-mechanical values is somewhat larger (~3 kJ/mole).

The dependence of the binding energy on the interwall distance is shown in Fig. 3. As it was noted earlier [28], the initial interwall distance (the distance between the midpoints of the walls) ΔR_{NT} is directly proportional to $n_2 - n_1$. The differences in the chirality indices Δn_{NT} for the considered double-walled nanotubes were selected in such a way as to convey a presumable minimum in the mentioned dependence. Comparison of molecular-mechanical and quantum-chemical results shows their qualitative agreement. It should be noted that at a large interwall distances both approaches lead to a distorted (oblate) form of the outer nanotube with a decrease in the interwall distance in some parts of the touching surfaces and with an increase in the others. According to the data of quantum-chemical calculations, the optimal distance between the walls in double-walled armchair tubes is 6.4 Å, which corresponds to Δn_{NT} = 7, 8, while the same distance in zigzag tubes is 6.2 Å, which approximately corresponds to Δn_{NT} = 13. Molecular-mechanical calculations give the following values: 6.2 Å (Δn_{NT} = 7) for armchair DWNTs and 6.0 Å (Δn_{NT} = 12, 13) for zigzag DWNTs.

Calculations of Multi-walled Nanotubes

In the Ref. [25] the HRTEM image of a 14-walled WS_2 nanotube with a "zigzag" chirality and an outer diameter of 30 nm is presented. Zigzag nanotubes with chiralities near (300, 0) have close diameters. A series of nanotubes with an outmost wall of chirality (298, 0) and a chirality step Δn_{NT} = 12 was chosen as the pattern for constructing possible simulation models. The specified parameters determine the following 14-walled nanotube (142, 0)@(154, 0)@(166, 0)@(178, 0)@(190, 0)@...@(286, 0)@(298, 0). At the present stage of the work, modeling of the internal part of a 14-walled NT formed by five SWNTs from (142, 0) to (190, 0) has been performed. Eventually, the sequence of MWNTs was considered from double-walled (142, 0)@(154, 0) to quintuple-walled (142, 0)@(154, 0)@(166, 0)@(178, 0)@(190, 0). The largest quintuple-walled zigzag NT contains 4980 atoms per unit cell (Fig. S1). To compare the properties of nanotubes with different types of chirality, we calculated a quintuple-walled armchair NT with a close outer diameter and Δn_{NT} = 7: (82, 82)@(89, 89)@(96, 96)@(103, 103)@(110, 110). The unit cell of such nanotube contains 2890 atoms (Fig. S2). As in the case of the quintuple-walled zigzag NT, we considered the corresponding series of single-wall and multi-walled armchair NTs coupled to the quintuple-walled "armchair" type nanotube. The diameters of the considered armchair nanotubes are close to the diameters of the corresponding zigzag nanotubes.

Figure 4 demonstrates cross-sections of optimized structures of triple-walled nanotubes of both types of chirality. It can be seen that the zigzag NT has a circular shape in cross section, while the armchair NT

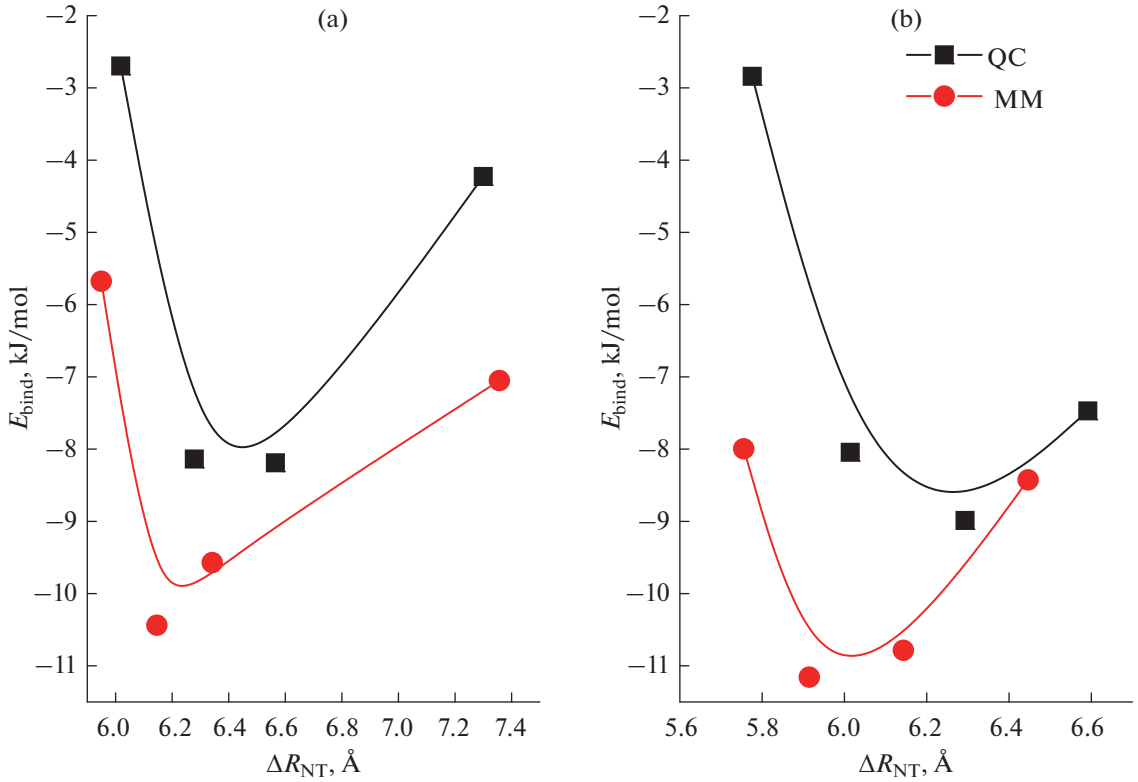

Fig. 3. Dependences of the binding energy of double-walled nanotubes WS_2 on the interwall distance: (a) "armchair" tubes; (b)—"zigzag" tubes. Designations: MM—results of calculations with the help of a force field; QC—results of quantum chemical calculations.

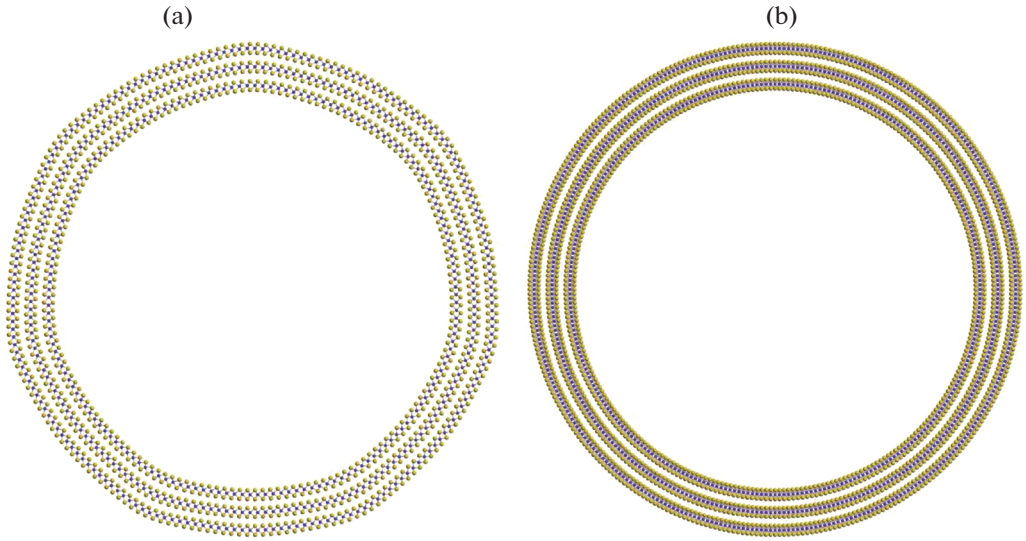

Fig. 4. Cross section of triple-walled nanotubes: (a)—chirality "armchair" (82, 82)@(89, 89)@(96, 96), (b)—chirality "zigzag" (142, 0)@(154, 0)@(166, 0). The structure is optimized by molecular mechanics. Light spheres are S atoms; dark spheres are W atoms.

acquires a faceted shape. All walls of MWNTs of the "armchair" type, starting from double-walled ones, have a similar faceted shape. This behavior of multiwalled nanotubes was observed earlier for a number of objects that we studied both quantum-chemically and molecular-mechanically using various force fields. The faceted shape of double-walled and triple-walled armchair nanotubes based on chalcogenides of various metals (for example, In_2STe [28] and SnS_2 [52]) was found by means of quantum-chemical calculations.

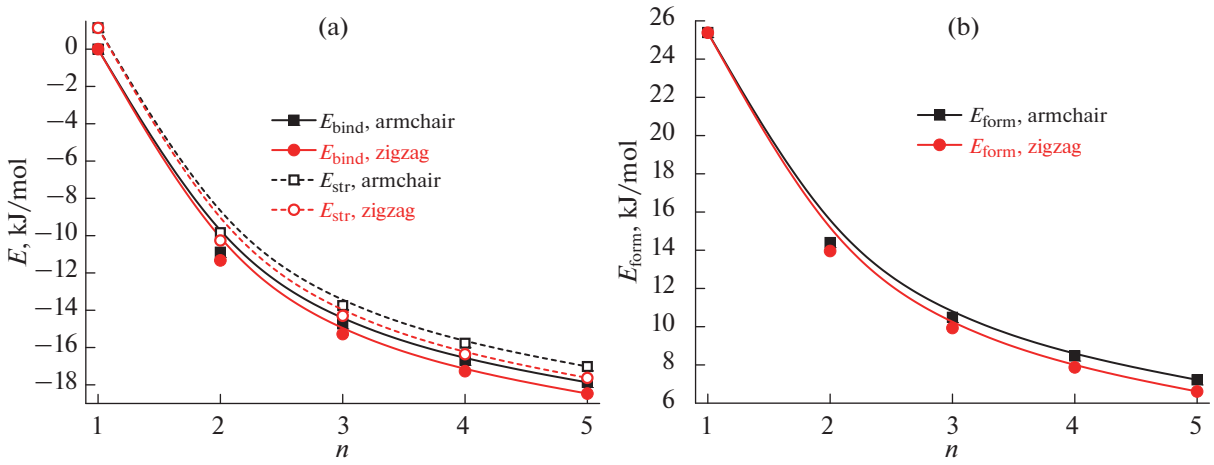

Fig. 5. Dependences of the binding energy (E_{bind}) and the formation energy from a monolayer (E_{str}) (a), as well as the formation energy from a bulk crystal (E_{form}) (b) on the number of walls in WS_2 multi-walled nanotubes. Molecular mechanical results for "armchair" and "zigzag" nanotubes are presented.

Simulations using force fields of multi-walled nanotubes based on MoS_2 [31], GaS, GaTe and Ga_2STe [34] revealed the same result.

The dependences of the binding energies (Eq. (4)), strain energies (Eq. (6)) and formation energies (Eq. (5)) on the number of walls of the considered nanotubes are shown in Fig. 5. The graphs presented indicate that already double-walled nanotubes are stable with respect to the monolayer. This result agrees with the conclusion obtained earlier by Seifert et al. [53] and confirms it. At the same time, WS_2 zigzag multi-walled nanotubes are more stable than armchair nanotubes, and the relative advantage of zigzag nanotubes increases with the number of walls. The energy of formation of multi-walled nanotubes from the bulk phase is positive and, obviously, tends to zero with increasing number of walls.

The important structural parameter of the multi-walled nanotubes is the interwall spacing. This parameter is experimentally measured and can serve as one of the criteria for the efficiency of the force field simulation quality. Table 2 shows the interwall distances for the studied multi-walled nanotubes. According to our simulation data, the interwall distances turn out to be maximal for the thinnest inner SWNT constituents, decreasing as their diameters increase, but increase again in the outer parts of multi-walled nanotubes. At the same time, the interwall distances in all MWNTs are greater than the distance between the layers of a bulk crystal, which is 6.162 Å [51]. Krause et al. [25] experimentally observed a change in the interwall distance in a multi-walled nanotube (30 walls, outer diameter 500 Å) depending on the location of the walls in the middle, on the inner or outer edges of the nanotube. However the indicated values [25] of the interwall spacing are quite large: from 6.84 to 6.41 Å. According to our data, the average interwall distances in zigzag nanotubes are 6.20 Å, and in armchair nanotubes, 6.25 Å. Our values almost coincide with the results of measurements in the study [20], where depending on the method of nanotube synthesis, the averaged interwall distances are 6.214 Å (method I) and 6.242 Å (method II).

Table 2. Interwall distances (ΔR_{NT}) in quintuple-walled nanotubes of chirality "armchair" (82, 82)@(89, 89)@(96, 96)@(103, 103)@(110, 110) and "zigzag" (142, 0)@(154, 0)@(166, 0)@(178, 0)@(190, 0)

Wall numbers for spacing	ΔR_{NT}, Å	
	armchair	zigzag
1-2	6.26	6.21
2-3	6.24	6.20
3-4	6.24	6.19
4-5	6.24	6.20
Average values:	6.25	6.20

The diameter of a single-wall NT changes when it becomes one of the walls of a multi-walled NT. Table 3 lists the diameters of free single-wall nanotubes and their diameters in the case when they are part of multi-walled nanotubes. According to our calculations, single-wall nanotubes shrink when entering the innermost part of the multi-walled nanotube. In the middle of a multi-walled nanotube, the changes in diameters are small, but as the outer surface is approached, the wall diameters begin to exceed the diameters of "free" NTs. It should be noted that these changes in diameters are very small and amount to tenths of a percent: 0.4–0.6%. Nevertheless, modern experimental methods make it possible to measure the diameter of nanotubes down to tenths of an angstrom (see Refs. [22, 24]), and, therefore, the diameter changes discussed can indeed be detected.

Table 3. Diameter (D_{NT}) of single-wall nanotubes in the free state and inside quintuple-walled nanotubes

Wall number	Armchair			Zigzag		
	chirality	D_{NT}, Å		chirality	D_{NT}, Å	
		free NT	inside MWNT		free NT	inside MWNT
1	(82, 82)	142.9	142.1	(142, 0)	143.0	142.2
2	(89, 89)	155.1	154.6	(154, 0)	155.0	154.7
3	(96, 96)	167.2	167.1	(166, 0)	167.1	167.1
4	(103, 103)	179.4	179.6	(178, 0)	179.1	179.4
5	(110, 110)	191.6	192.1	(190, 0)	191.1	191.8

CONCLUSIONS

A technique for creating a force field for modeling nanosystems has been proposed, which has been successfully applied to calibrate atomic potentials describing interactions in bulk phases, nanolayers, and nanotubes based on WS_2.

Using a developed force field, the structure and stability of nanotubes with "armchair" and "zigzag" chiralities in series from single-wall to quintuple-walled were calculated for the first time. Quintuple-walled nanotubes of both chirality types have close inner (142 Å) and outer (192 Å) diameters. The interwall distances of multi-walled nanotubes obtained during the simulation agree well with the results of recent measurements of these parameters. Zigzag nanotubes have lower binding, strain, and formation energies than the corresponding energies of armchair nanotubes and are therefore more stable. Perhaps this is due to the fact that the interwall interaction in zigzag tubes is greater than the interwall interaction in armchair tubes. For the same reason, "zigzag" type nanotubes have a circular cylindrical structure with dense wall packing, while "armchair" type nanotubes have a faceted cylinder structure with looser packing.

ACKNOWLEDGMENTS

The authors thank the Resource Center "Computer Center of St. Petersburg State University" for providing the computational facilities and help in the accomplishment of the high producible calculations.

FUNDING

This work was financially supported by the Russian Science Foundation (RSF) within the framework of research project no. 23-23-00040, https://rscf.ru/project/23-23-00040/.

CONFLICT OF INTEREST

The authors declare that they have no conflicts of interest.

SUPPLEMENTARY INFORMATION

The online version contains supplementary materials available at https://doi.org/10.1134/S003602362360209X.

Supporting information includes:

Table S1. The SWMBL-C force field parameters.

Table S2. Comparison of the properties of WS_2 2*H* and 3*R* bulk phases, monolayer and nanotubes (12, 12), (6, 6), measured experimentally or calculated by DFT method with the results of modeling by molecular mechanics using the proposed force field.

Table S3. Comparison of the phonon frequencies (cm^{-1}) at the Γ point of the Brillouin zone for the 2*H*-WS_2 crystal, measured experimentally and calculated by DFT method, with the results of modeling by the molecular mechanics using the proposed force field.

Fig. S1. Cross-sectional view of the force-field optimized structure of a WS_2 5-walled NT (82, 82)@(89, 89)@(96, 96)@(103, 103)@(110, 110) with armchair chirality.

Fig. S2. Cross-sectional view of the force-field optimized structure of a WS_2 5-walled NT (142, 0)@(154, 0)@(166, 0)@(178, 0)@(190, 0) with zigzag chirality.

REFERENCES

1. J. L. Musfeldt, Y. Iwasa, and R. Tenne, Phys. Today **73**, 42 (2020). https://doi.org/10.1063/PT.3.4547
2. H. Kawai, M. Sugahara, R. Okada, et al., Appl. Phys. Express **10**, 015001 (2017). https://doi.org/10.7567/APEX.10.015001
3. B. Kim, N. Park, and J. Kim, Nat. Commun. **13**, 3237 (2022). https://doi.org/10.1038/s41467-022-31018-8
4. K. R. O'Neal, J. G. Cherian, A. Zak, et al., Nano Lett. **16**, 993 (2016). https://doi.org/10.1021/acs.nanolett.5b03996
5. S. S. Sinha, A. Zak, R. Rosentsvieg, et al., Small **16**, 1904390 (2020). https://doi.org/10.1002/smll.201904390
6. K. S. Nagapriya, O. Goldbart, I. Kaplan-Ashiri, et al., Phys. Rev. Lett. **101**, 195501 (2008). https://doi.org/10.1103/PhysRevLett.101.195501
7. R. Levi, O. Bitton, G. Leitus, et al., Nano Lett. **13**, 3736 (2013). https://doi.org/10.1021/nl401675k
8. M. Sugahara, H. Kawai, Y. Yomogida, et al., Appl. Phys. Express **9**, 075001 (2016). https://doi.org/10.7567/APEX.9.075001

9. F. Qin, W. Shi, T. Ideue, et al., Nat. Commun. **8**, 14465 (2017). https://doi.org/10.1038/ncomms14465
10. C. Y. Zhang, S. Wang, L. J. Yang, et al., Appl. Phys. Lett. **100**, 243101 (2012). https://doi.org/10.1063/1.4729144
11. Y. J. Zhang, M. Onga, F. Qin, et al., 2D Mater. **5**, 035002 (2018). https://doi.org/10.1088/2053-1583/aab670
12. Y. Divon, R. Levi, J. Garel, et al., Nano Lett. **17**, 28 (2017). https://doi.org/10.1021/acs.nanolett.6b03012
13. D. Maharaj and B. Bhushan, Tribol. Lett. **49**, 323 (2013). https://doi.org/10.1007/s11249-012-0071-0
14. C. S. Reddy, A. Zak, and E. Zussman, J. Mater. Chem. **21**, 16086 (2011).
15. E. Zohar, S. Baruch, M. H. Shneider, et al., J. Adhes. Sci. Technol. **25**, 1603 (2011). https://doi.org/10.1163/ 016942410X524138
16. G. Otorgust, H. Dodiuk, S. Kenig, and R. Tenne, Eur. Polym. J. **89**, 281 (2017). https://doi.org/10.1016/j.eurpolymj.2017.02.027
17. L. Yadgarov, B. Višić, T. Abir, et al., Phys. Chem. Chem. Phys. **20**, 20812 (2018). https://doi.org/10.1039/c8cp02245c
18. Md. A. Rahman, Y. Yomogida, M. Nagano, et al., Jpn. J. Appl. Phys. **60**, 100902 (2021). https://doi.org/10.35848/1347-4065/ac2013
19. G. Shen, Y. Yan, and K. Hong, Mater. Lett. **319**, 132303 (2022). https://doi.org/10.1016/j.matlet.2022.132303
20. S. S. Sinha, L. Yadgarov, S. B. Aliev, et al., J. Phys. Chem. **125**, 6324. https://doi.org/10.1021/acs.jpcc.0c10784
21. Y. Yomogida, Y. Miyata, and K. Yanagi, Appl. Phys. Express **12**, 085001 (2019). https://doi.org/10.7567/1882-0786/ab2acb
22. SadanM. Bar, L. Houben, A. N. Enyashin, et al., PNAS **105**, 15643 (2008). https://doi.org/10.1073/pnas.0805407105
23. H. Deniz and L.-C. Qin, Chem. Phys. Lett. **552**, 92 (2012). https://doi.org/10.1016/j.cplett.2012.09.041
24. Y. Chen, H. Deniz, and L.-C. Qin, Nanoscale **9**, 7124 (2017). https://doi.org/10.1039/c7nr01688c
25. M. Krause, A. Mücklich, A. Zak, et al., Phys. Status Solidi B **248**, 2716 (2011). https://doi.org/10.1002/pssb.201100076
26. G. Seifert, H. Terrones, M. Terrones, et al., Solid State Commun. **114**, 245 (2000). https://doi.org/10.1016/S0038-1098(00)00047-8
27. M. Ghorbani-Asl, N. Zibouche, M. Wahiduzzaman, et al., Sci. Rep. **3**, 2961 (2013). https://doi.org/10.1038/srep02961
28. A. V. Bandura, D. D. Kuruch, S. I. Luk'yanov, and R. A. Evarestov, Russ. J. Inorg. Chem. **67**, 2009 (2022). https://doi.org/10.1134/S0036023622601970
29. R. A. Evarestov, A. V. Bandura, V. V. Porsev, and A. V. Kovalenko, J. Comput. Chem. **38**, 2581 (2017). https://doi.org/10.1002/jcc.24916
30. R. A. Evarestov, A. V. Kovalenko, A. V. Bandura, et al., Mater. Res. Express **5**, 115028 (2018). https://doi.org/10.1088/2053-1591/aadf00
31. A. V. Bandura, S. I. Lukyanov, D. D. Kuruch, and R. A. Evarestov, Physica E **124**, 114183 (2020). https://doi.org/10.1016/j.physe.2020.114183
32. S. Piskunov, O. Lisovski, Y. F. Zhukovskii, et al., ACS Omega **4**, 1434 (2019). https://doi.org/10.1021/acsomega.8b03121
33. J. A. Talla, Kh. Al-Khaza'leh, and N. Omar, Russ. J. Inorg. Chem. **67**, 1025 (2022). https://doi.org/10.1134/S0036023622070178
34. S. I. Lukyanov, A. V. Bandura, R. A. Evarestov, et al., Physica E **133**, 114779 (2021). https://doi.org/10.1016/j.physe.2021.114779
35. R. Dovesi, A. Erba, R. Orlando, et al., WIREs Comput. Mol. Sci. **8** (2018). https://doi.org/10.1002/wcms.1360
36. R. Dovesi, V. R. Saunders, C. Roetti, et al., *CRYSTAL 17 User's Manual* (University of Turin, Torino, 2018).
37. L. F. Pacios and P. A. Christiansen, J. Chem. Phys. **82**, 2664 (1985). https://doi.org/10.1063/1.448263
38. R. B. Ross, J. M. Powers, T. Atashroo, et al., J. Chem. Phys. **93**, 6654 (1990). https://doi.org/10.1063/1.458934
39. J. Heyd, G. E. Scuseria, and M. Ernzerhof, J. Chem. Phys. **118**, 8207 (2003). https://doi.org/10.1063/1.1564060
40. H. J. Monkhorst and J. D. Pack, Phys. Rev. B **13**, 5188 (1976). https://doi.org/10.1103/PhysRevB.13.5188
41. S. Grimme, J. Comput. Chem. **27**, 1787 (2006). https://doi.org/10.1002/jcc.20495
42. J. D. Gale and A. L. Rohl, Mol. Simul. **29**, 291 (2003). https://doi.org/10.1080/0892702031000104887
43. S. Shi, L. Yan, Y. Yang, et al., J. Comput. Chem. **24**, 1059 (2003). https://doi.org/10.1002/jcc.10171
44. A. Krishnamoorthy, A. Mishra, D. Kamal, et al., SoftwareX **13**, 100663 (2021). https://doi.org/10.1016/j.softx.2021.100663
45. K. Nomura, R. K. Kalia, A. Nakano, et al., SoftwareX **11**, 100389 (2020). https://doi.org/10.1016/j.softx.2019.100389
46. Platypus. https://github.com/Project-Platypus/Platypus (accessed May 23, 2023).
47. M. L. Waskom, J. Open Source Soft **6**, 3021 (2021). https://doi.org/10.21105/joss.03021
48. J. D. Hunter, Comput. Sci. Eng. **9**, 90 (2007). https://doi.org/10.1109/MCSE.2007.55
49. *The pandas Development Team. Zenodo 2023*, pandas-dev/pandas: Pandas (v2.0.1). https://doi.org/10.5281/zenodo.7857418
50. F. Pedregosa, G. Varoquaux, A. Gramfort, et al., J. Machine Learning Res. **12**, 2825 (2011). https://doi.org/10.48550/arXiv.1201.0490
51. W. J. Schutte, J. L. De Boer, and F. Jellinek, J. Solid State Chem. **70**, 207 (1987). https://doi.org/10.1016/0022-4596(87)90057-0
52. A. V. Bandura and R. A. Evarestov, Sur. Sci. **641**, 6 (2015). https://doi.org/10.1016/j.susc.2015.04.027
53. G. Seifert, T. Köhler, and R. Tenne, J. Phys. Chem. B **106**, 2497 (2002). doi.org/ https://doi.org/10.1021/jp0131323

SPELL: OK